Chemico-Biological Interactions 394 (2024) 110977

Contents lists available at ScienceDirect

Chemico-Biological Interactions

journal homepage: www.elsevier.com/locate/chembioint

Research paper

Genotoxicity and heating Performance of $V_xFe_{3-x}O_4$ nanoparticles in Health applications

Beatriz Sanz-Sagué [a,1], Amaia Sáenz- Hernández [a], Ana C. Moreno Maldonado [a,b], Jesús A. Fuentes-García [a,b], Jorge M. Nuñez [a,b,c], Bojana Zegura [d,e,f], Alja Stern [d,e,f], Katja Kolosa [d], Iza Rozman [d,e,f], Teobaldo E. Torres [a,b,c], Gerardo F. Goya [a,b,*]

[a] Instituto de Nanociencia y Materiales de Aragón (INMA), CSIC-Universidad de Zaragoza, C/M Esquillor S/N, 50018, Zaragoza, Spain
[b] Departamento de Física de La Materia Condensada, Facultad de Ciencias, C/ Pedro Cerbuna 12, 50009, Zaragoza, Spain
[c] Laboratorio de Microscopías Avanzadas (LMA), Universidad de Zaragoza, C/Mariano Esquillor, 50018, Zaragoza, Spain
[d] National Institute of Biology, Department of Genetic Toxicology and Cancer Biology, Večna Pot 121, 1000, Ljubljana, Slovenia
[e] University of Ljubljana, Kongresni Trg 12, 1000, Ljubljana, Slovenia
[f] Biotechnical Faculty, University of Ljubljana, Jamnikarjeva ulica 101, 1000, Ljubljana, Slovenia

ARTICLE INFO

Keywords:
Magnetic nanoparticles
Vanadium ferrite
Cytotoxicity
Genotoxicity
Specific power absorption
Cell viability

ABSTRACT

The applications of magnetic nanoparticles (MNPs) as biocatalysts in different biomedical areas have been evolved very recently. One of the main challenges in this field is to design affective MNPs surfaces with catalytically active atomic centres, while producing minimal toxicological side effects on the hosting cell or tissues. MNPs of vanadium spinel ferrite (VFe_2O_4) are a promising material for mimicking the action of natural enzymes in degrading harmful substrates due to the presence of active V^{5+} centres. However, the toxicity of this material has not been yet studied in detail enough to grant biomedical safety. In this work, we have extensively measured the structural, compositional, and magnetic properties of a series of $V_xFe_{3-x}O_4$ spinel ferrite MNPs to assess the surface composition and oxidation state of V atoms, and also performed systematic and extensive *in vitro* cytotoxicity and genotoxicity testing required to assess their safety in potential clinical applications. We could establish the presence of V^{5+} at the particle surface even in water-based colloidal samples at pH 7, as well as different amounts of V^{2+} and V^{3+} substitution at the A and B sites of the spinel structure. All samples showed large heating efficiency with Specific Loss Power values up to 400 W/g ($H_0 = 30$ kA/m; $f = 700$ kHz). Samples analysed for safety in human hepatocellular carcinoma (HepG2) cell line with up to 24h of exposure showed that these MNPs did not induce major genomic abnormalities such as micronuclei, nuclear buds, or nucleoplasmic bridges (MNIs, NBUDs, and NPBs), nor did they cause DNA double-strand breaks (DSBs) or aneugenic effects—types of damage considered most harmful to cellular genetic material. The present study is an essential step towards the use of these type of nanomaterials in any biomedical or clinical application.

1. Introduction

Spinel ferrites have generated considerable interest within the scientific community since the 1950s due to their magnetic properties [1–3]. They are widely used in number of technological applications including spintronics devices, permanent magnets, microwave devices, data storage, magnetic catalysts and drug delivery [4,5]. Vanadium ferrite (VFe_2O_4), however, has been less studied despite its potential catalytic and enzymatic properties due to the presence of Vanadium in different oxidation states [6]. One of the earliest studies on VFe_2O_4 ferrite was conducted by V.M. Goldschmidt [7,8] who characterized its crystal structure and basic physical properties. Since then, a rather low number of studies on VFe_2O_4 ferrite have been reported compared to other spinel oxides. However, the complete solubility of V in the Fe sublattice of the spinel structure, together with the different oxidation states of Vanadium, make this compound very interesting in terms of magnetic and electrical properties, with potential applications in various fields such as catalysis and clinical uses. Additionally, the possibility of

* Corresponding author. Instituto de Nanociencia y Materiales de Aragón (INMA), CSIC-Universidad de Zaragoza, c/M Esquillor S/N, 50018, Zaragoza, Spain.
E-mail address: goya@unizar.es (G.F. Goya).
[1] Currently at BEOnChip S.L., Zaragoza, Spain.

https://doi.org/10.1016/j.cbi.2024.110977
Received 28 December 2023; Received in revised form 10 March 2024; Accepted 26 March 2024
Available online 27 March 2024

having active V^{5+} centres added to its magnetic properties could allow to mimic the capabilities of V_2O_5 oxide for advanced oxidation of organic pollutants in wastewater [9], which makes $V_xFe_{3-x}O_4$ spinel ferrite appealing. Indeed, the ability of V_2O_5 nanowires to have catalytic peroxidase-like activity on several substrates has been demonstrated [10].

The production of reactive oxygen species (ROS) of VFe_2O_4 under UV light is believed to originate from electron-hole pairs generated that promote the formation of highly reactive superoxide ions ($^{\bullet}O^{2-}$) and hydroxyl radicals ($^{\bullet}OH$). Also, the energy gap (1.5–2.5 eV) of $V_xFe_{3-x}O_4$ can be tuned by changing the size or composition of the MNPs allowing their photocatalytic properties to operate under sunlight. Since the amount of ROS produced under visible light is much lower than under UV irradiation, the optimization of the electronic structure providing an efficient band gap to operate under natural sunlight is appealing.

Regarding potential human uses, Vanadium spinel nanoparticles have been found to impact several biochemical processes, including mitogenic properties in various cell types, as well as the ability to alter enzymatic activities and play a key role in the optimal growth of chicks and rats [11]. *In vivo* experiments conducted in the early 1970s confirmed the essentiality of vanadium, raising interest in its physiological effects and toxicity in humans. An interesting property of vanadium is related to its insulin-like effects, first reported in the '80s [12,13], showing that vanadate could stimulates glucose uptake and oxidation in rat adipocytes, through a mechanism related to the cytoplasmic domain of the β−subunit of the insulin receptor tyrosine kinase [14]. Vanadate also stimulates glycogen synthase in rat adipocytes and skeletal muscle and increases translocation of the Type II insulin-like growth factor receptor [15]. Few previous works related to biological applications include their study as detectors of dopamine neurotransmitter [16] but studies for human use are scarce. There are no previously reported studies on the cytotoxicity of Vanadium ferrite MNPs, although a recent work reported on the toxicity of VO_2 nanoparticles in human lung [17]. In this work, we present a systematic study of the structural and magnetic properties of $V_xFe_{3-x}O_4$ nanoparticles, together with extensive cytotoxicity and genotoxicity *in vitro* tests, as a prerequisite for potential human use in future biocatalytic applications. To this aim, we present magnetic and toxicological data on three types of $V_xFe_{3-x}O_4$ spinel oxide magnetic nanoparticles.

2. Results and discussion

2.1. Structural and physicochemical properties

The spinel structure of the MNPs was confirmed from the XRD patterns (Fig. 1). The observed peaks could be related to theoretical positions and intensities of the crystalline planes in the spinel Fe_3O_4 structure with Miller indices (111), (220), (311), (222), (400), (422), (511), (440), (531), (620), (533), (622), (444), and (642), according with the JCPDS card 19–629. The synthesis route, a modified protocol from Massart and Cabuil [18], ended in a host spinel structure substituted with Vanadium ions from the VCl_3 precursor. No detectable reflections from V oxides were observed but it is possible to observe localized and sharpen reflections as the amount of VCl_3 in the samples increases. These results can be explained by better crystallization and incorporation of V atoms within the host network during the nucleation and growth of the MNPs.

Transmission electron microscopy (TEM) images showed that all samples were composed of well-defined faceted MNPs with definite cubic/octahedral shape (Fig. 2). The analysis of the images provided the histograms of the particle distribution of all three samples. Fitting the histograms with a Gaussian distribution yielded the average sizes <d> and standard deviation σ for the three samples shown in Table 1. These values indicated an increase in the mean size values with increasing V contents. The stoichiometry of samples V01, V02, and V03 were obtained by collecting Energy-Dispersive X-ray Spectroscopy

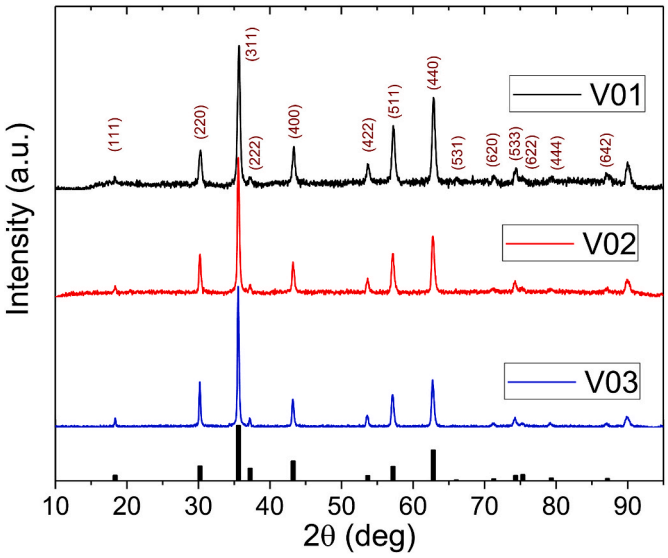

Fig. 1. X-diffraction data of samples V01, V02 and V03. Lowest panel: theoretical positions and intensities (normalized) expected from Fe_3O_4. Miller indices are in parenthesis (h k l).

(EDX) spectra from different macroscopic (≈1 × 1 μm^2) regions of the samples, providing compositional information from a sample volume of ≈1–3 μm^3. Averaging SEM-EDX spectra over a minimum of five areas from each sample (Fig. S1 in the Supplementary Material) yielded the composition summarized in Table 1.

Electron energy-loss spectra (EELS) analysis was used (Fig. 3) to assess the chemical composition of the samples at the single-particle level, by obtaining the corresponding elemental mapping (Fig. 3c–f) with the spatial distribution of elements for the sample.

The EELS-SI profiles allowed for the assessment of vanadium's concentration at the single particle level, with a constant concentration across the whole single particle profiles measured (Fig. 3b). For sample V01 the vanadium signal was slightly above the detection levels, with a resulting atomic percentage of 3–5 at % for V, in agreement with the EDX-SEM data from powder ('bulk') samples shown in Table 1. This concentration is consistent with the low intensity of the corresponding absorption edge in the spectra recorded (see Fig. S2 in the Supplementary Material). In samples V02 and V03, with larger V contents, a reduced energy dispersion ratio of 0.1 for the EELS examination could be implemented aiming to attenuate the signal-to-noise ratio for the quantification of vanadium (Fig. S3 in Supplementary Material).

The analysis of the actual oxidation states of V was performed through the absorption edges within the typical energy range between 513 and 521 eV for the different vanadium species. The results are shown in Fig. 4.

Further information on the surface composition of the nanoparticles was obtained from XPS measurements, through the kinetic energy of the photoelectrons emitted as a function of the binding energy. In Fig. 5 (first left column) the interactions corresponding to the elements iron, oxygen and vanadium are shown. The assignment of these absorption edges is as follows: 284.8 eV (C 1s); 983.7, 531.0 eV (O KLL, O 1s); 846.0, 786.7, 711.0, 729.0, 95.0, 56 eV (Fe 2s, Fe LMM, Fe 2p1/2, Fe 2p3/2, Fe 3s, Fe 3p); 1017.7, 628.0, 520.0, 513.0 eV (V LMM, V 2s, V 2p1/2, V 2p3/2). The quantitative analysis (Table S1 of the Supplementary Material) confirmed the increasing contents of V in the Fe/V a. t % ratios form 98.5/1.5 in sample V01; 97.5/2.5 in V02; and 97/3 in V03, consistent with the incorporation of V into the spinel crystal lattice.

The distribution of cations in spinel ferrites of formula AB_2O_4 can be related to their enthalpy of formation. These enthalpies have been determined to derive empirical site preference energies, especially for the composition $A^{2+}B_2^{3+}O_4$ (known as 2–3 type spinel) and, in less

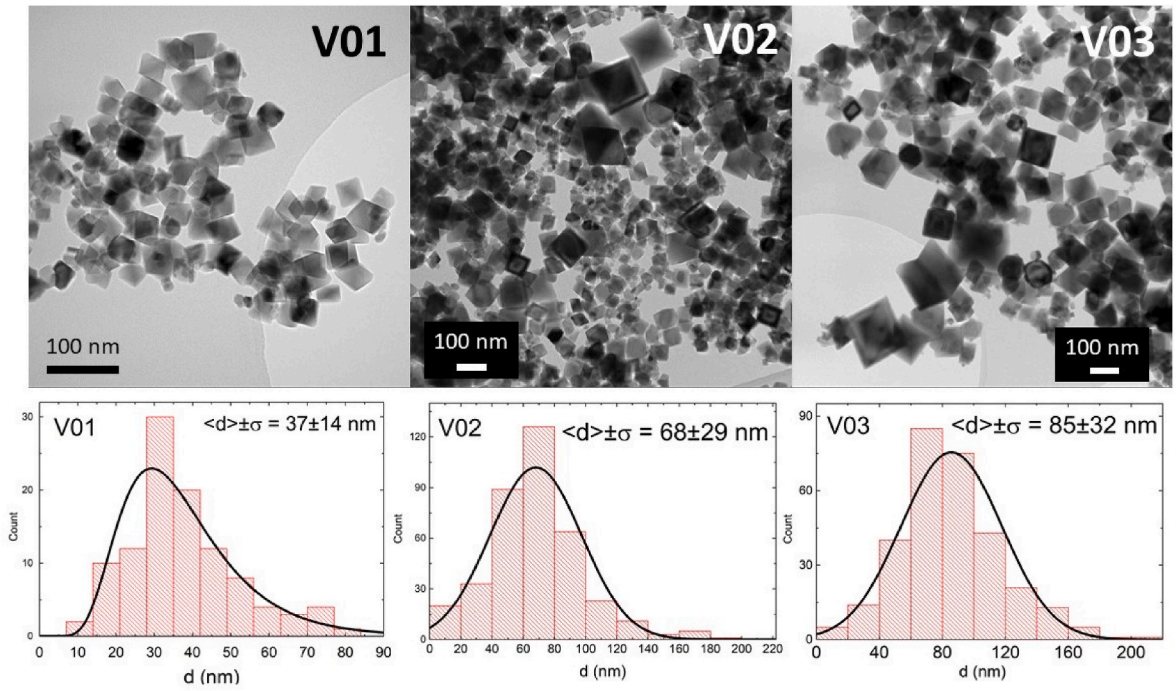

Fig. 2. TEM images of samples V01, V02 and V03 (top panel) and the corresponding size distribution histograms (bottom panel).

Table 1
Compositional values from SEM-EDX analysis of samples $V_xFe_{3-x}O_4$. Average size (<d>), distribution width (±σ), coercive field (H_C) and saturation magnetization (M_S) at T = 295 K.

Sample	$V_xFe_{3-x}O_4$ (nominal)	$V_xFe_{3-x}O_4$ (experimental)	<d>±σ (nm)	H_C (kA. m^{-1})	M_S (emu. g^{-1})
V01	$V_{0.1}Fe_{2.9}O_4$	$V_{0.10}Fe_{2.90}O_4$	37 ± 14	6.4 ± 0.4	64.5 ± 0.1
V02	$V_{0.2}Fe_{2.8}O_4$	$V_{0.20}Fe_{2.80}O_4$	68 ± 29	7.0 ± 0.5	63.1 ± 0.1
V03	$V_{0.3}Fe_{2.7}O_4$	$V_{0.27}Fe_{2.73}O_4$	85 ± 32	7.9 ± 0.5	53.8 ± 0.1

amount, for the 2–4 spinel type ($A^{4+}B_2^{2+}O_4$) [19]. Since the two ferromagnetic sublattices in Fe_3O_4 formed by the A and B sites have a weaker A-B (antiferromagnetic) interaction, the weaker Fe^{3+}- Fe^{2+} coupling makes the magnetite lattice susceptible to the influence of V ions. Accordingly, it is observed that the interactions of the Fe^{3+} and Fe^{2+} oxidation states are increasingly modified for increasing contents of V in the samples. Comparatively (Table S2 of Supplementary Material), the band corresponding to the Fe^{3+} interactions decreases with increasing vanadium contents, while the band Fe^{2+} increases and the satellite band decreases [20], indicating a more crystalline structure.

Many Vanadium oxides have been reported to present an absorption edged within the 540 - 510 eV energy range [21] but the intensities of the O 1s associated photoelectrons are much higher than the V oxidation states bonded. Therefore, for a better analysis this energy range has been separated in two. From 535 to 525 eV (Fig. 5c–g, k) interval, the O 1s photoelectron interactions in the network produce a band at ≈530 eV that can be deconvoluted in three bands, one explained by the lattice bonded oxygen (530.26 eV), other for hydroxide related (531.4 eV) and another for adsorbed water and organic compounds at 533 eV. The splatted bands from V01 and V02 (Fig. 5 c, g) produce more hydroxide-related binding energy intensities, while the lattice related photoelectron band have more localized at 530.26 eV maximum in the V03 sample (Fig. 5 k). From the analysis of the V2 p1/2 and V 2p3/2 regions from 530 to 510 eV (Fig. 5 d, h, l), the oxidation states of V can be resolved, and the splatted bands suggest the presence of V (II), V (III), V (IV) and V (V) on the surface of the samples. In the spinel structure, the V atoms occupy the tetrahedral sites by the V(IV) oxidation state, and the octahedral sites have an oxidation state of V(III). On the other hand, V (II) and V (V) oxidation states can be attributed to surface bearing Fe–V bindings [22]. The results suggest a better incorporation of the V atoms in the spinel lattice as the VCl_3 amount increases, but more reactive surfaces on MNPs can be produced by the V01 samples because of the presence of different oxidation states.

The M vs. T data taken in zero-field-cooling and field-cooling modes (Fig. 6) showed the expected absence of a definite blocking temperature, since the average particle sizes observed from TEM images imply that the MNPs are well above the single-domain size for these small V concentrations in the spinel structure. Consistently, the steep increase in M (T) data observed at T ≈ 20 K could be assigned to a shifted Verwey transition due to Vanadium doping within the Fe_3O_4 lattice ($T_V \approx 129$ K for bulk Fe_3O_4).

The hysteresis cycles M *vs*. H measured at room temperature (Fig. S4 in Supplementary Material) showed a measurable coercive field for all samples, suggesting that a blocked state or multidomain structure is present. The coercive fields H_C (see Table 1) are essentially the same within error, while the saturation magnetization M_S reflects the reduction induced by the incorporation of nonmagnetic V into the lattice, especially for the highest concentration of x = 0.3. A slight but measurable non-saturation for large fields was noticeable (slope of $\approx 10^{-4}$ emu/g.Oe) in all samples that could originate from spin canting effects induced by vanadium since surface effects (i.e. spin disorder) can be neglected due to the large size of the MNPs.

Regarding the heating capacity of our MNPs, equation (2) provides the calorimetric formula for determining the Specific Loss Power (SLP) as the main physical parameter that represents the heating ability at a particular magnetic field amplitude and frequency, given in Watts per gram (W/g) of magnetic material

$$SLP = \frac{m_l\, c_l + m_{NP}\, c_{NP}}{m_{NP}} \left(\frac{dT}{dt}\right)_{max} \quad \text{Eq. (2)}$$

where m_l and m_{NP} are the mass of the solvent and the nanoparticles,

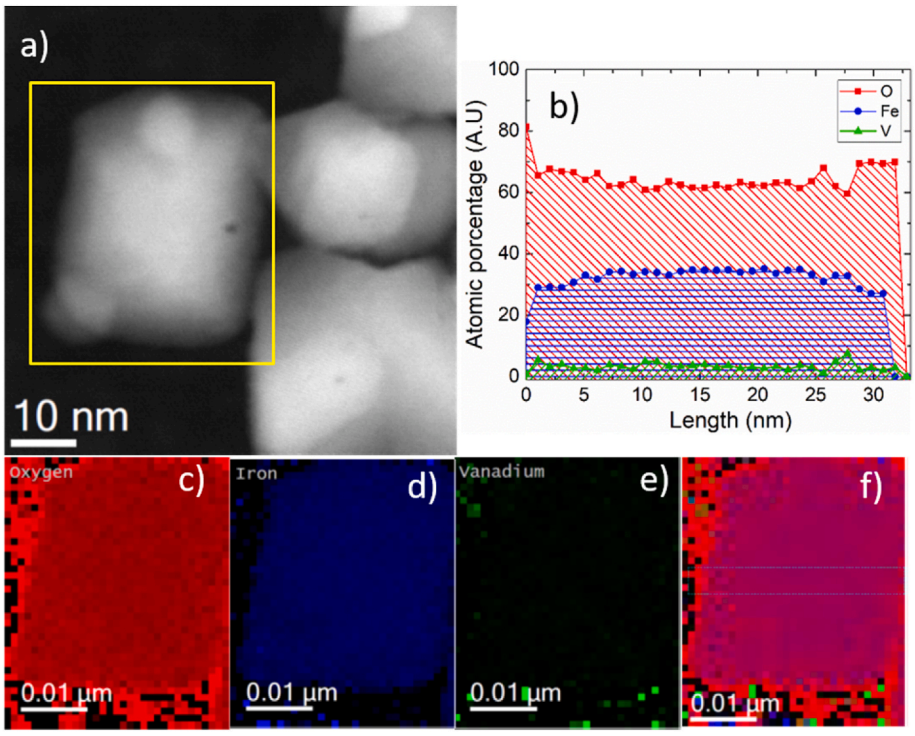

Fig. 3. Elemental mapping performed using EELS-SI on an isolated particle in V01 sample ($V_{0.1}Fe_{2.9}O_4$) a) typical STEEM-HAADF image b) Line profile across the NP, extracted from this EELS dataset and of the atomic percentages c) O in red d) Fe in blue e) V in green and f) composition maps.

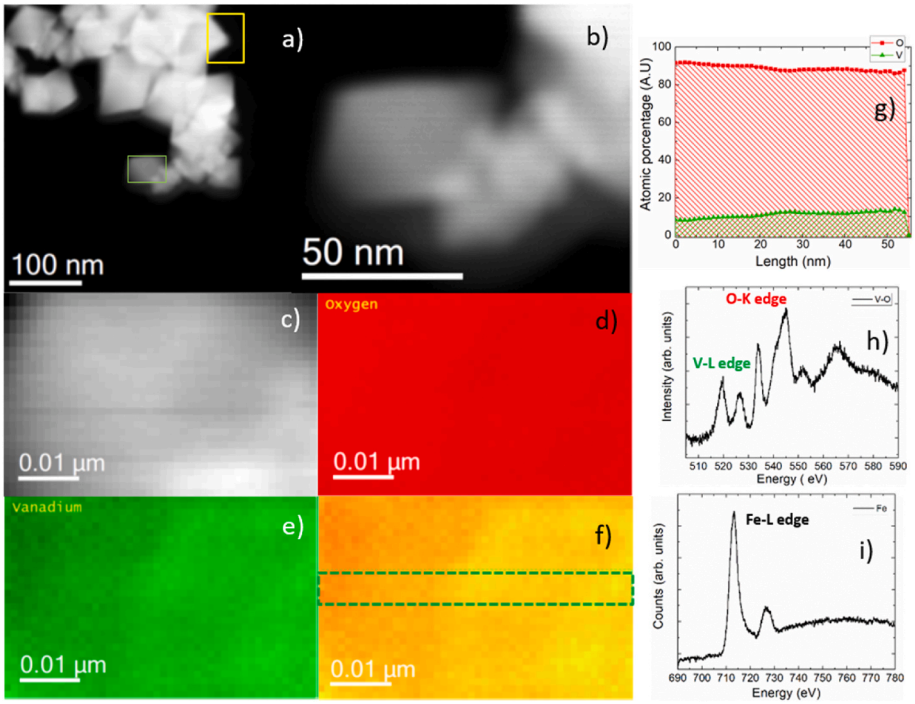

Fig. 4. Elemental EELS-SI mapping for an individual NP of V03 sample ($V_{0.3}Fe_{2.7}O_4$). a) Typical STEEM-HAADF image chosen for the analysis (green rectangle) with the region taken as a reference to avoid drift during the experiment (yellow rectangle) b) Zoom of the analysis area depicted in a, with the corresponding EELS-Spectrum image (c) and the elemental mapping for oxygen (d, red), vanadium (e, green) and iron (f, yellow). The compositional line profile across the NP from the composition map (g). The EELS spectra of SI with the V–O–K edge (523 and 532 eV) and Fe–L (713 eV) edges are shown in panels h, and I, respectively.

respectively, while c_l and c_{NP} are the specific heat of the solvent (water, $c_l = 4.186$ J/g.K) and the MNPs ($c_{NP} = 0.65$ J/g.K). The heating rate of the sample, dT/dt, was determined from the sequential magnetic field pulses at the point of maximum slope (Figs. S5 and S6 in the Supplementary Material).

All measurements have been done with the MNPs immobilized in gelatin to block the Brownian relaxation contribution to the SLP, leaving only the Néel relaxation mechanism, as these conditions serve to display

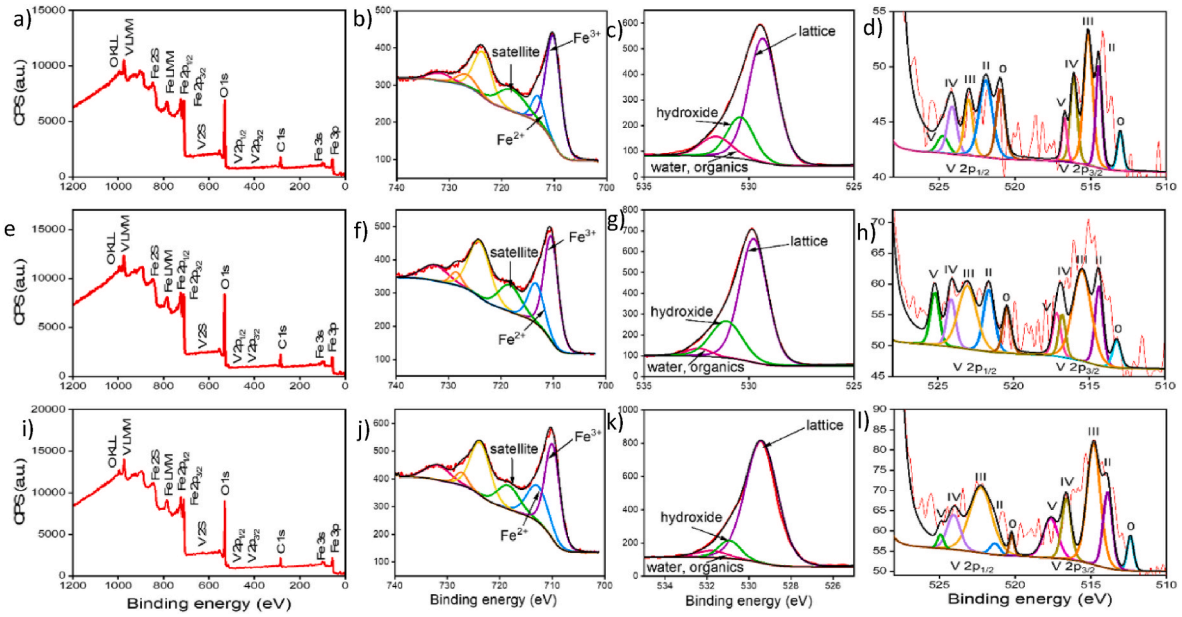

Fig. 5. XPS spectra of $V_xFe_{3-x}O_4$ samples. Left column: wide-view from 1200 to 0 eV of samples V01 (a), V02 (e) and V03 (i). The energies for Fe^{3+} and Fe^{2+} are shown for the Fe2p region (740-700 eV) in b, f, and j. Oxygen O 1s interactions were fitted in the 535-325 eV interval (c, g, k). The different Vanadium oxidation states (d, h, l) corresponded to V (II), V (III), V (IV) and V (V) on the surface of the samples.

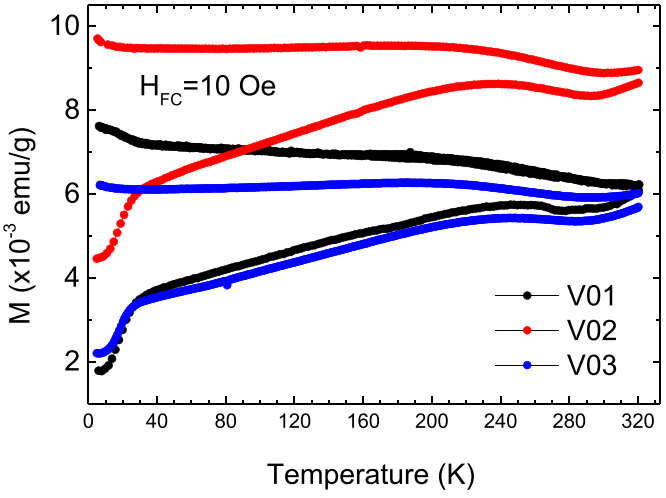

Fig. 6. Zero field cooled and field cooled curves (HFC = 10 Oe) for samples V01, V02 and V03.

a more accurate SLP value that will be found under the high viscosity conditions of the intracellular media in biomedical applications. Estimates of intracellular viscosity vary widely, but it is generally accepted to be in the range of ≈140 cP (0.14 Pa s), depending on the cell type and intracellular compartment [23]. Additionally, the immobilization of the MNPs in a gelatine matrix allows successive experiments on a single sample and, more importantly, eliminates the errors introduced by sample precipitation and chain formation induced by the applied field [24] that modify the observed SLP values [25], as well as changes in MNPs concentration (solvent evaporation) during experiments.

The SLP dependence with magnetic field amplitude H_0, ($f = 299.15$ kHz) showed a saturation of the values at high fields for V02 and V03 samples (Fig. 7). Attempts to fit the data within the whole H_0 range with the allometric-type equation $SLP(H) = A\,H^{\lambda}$, where A and λ are free parameters [26], yielded poor results. This allometric dependence, with $\lambda = 2$, would be expected within the Linear Response Theory (LRT), applicable when the condition $k_BT < M_S\mu_0VH_0$ is fulfilled. The observed deviation from this expression can be expected for large particles that departs from the single-domain magnetic configuration. We hypothesize that the large volume (V) of the present MNPs makes the LRT not applicable, possibly due to nonlinear spin (or multidomain) magnetic configurations of the larger MNPs particles V02 and V03. Consistently, the allometric fit performed within the low-H_0 region yielded the same $\lambda = 2.9 \pm 0.1$ for all samples. However, a sigmoidal fit was required to fit the whole H_0 experimental range. We used a generalization of the Gompertz distribution (the shifted Gompertz function),

$$SLP(H) = A\,e^{-\left[e^{-k(H-H_C)}\right]} \qquad \text{Eq. (3)}$$

where A is the amplitude (SLP at infinite H_0), k is the parameter for SLP change rates, and H_C is the field at maximum growth of the SLP. This expression allows us to identify the maximum SLP expected until saturation, and the optimal H_0 applied field needed to obtain the maximum $\frac{SLP}{H_0}$ ratio as a useful parameter to avoid overestimated intensities that result in wasted power. This point could be established as a percentage of the A values, somewhere between H_C and the saturation region for instance, 90% of the asymptotic SLP value would occur for $H = H_C - \frac{2.25}{k}$.

It is clear from Fig. 7 and Table 2 that the maximum expected SLP amplitudes decrease with increasing V contents and particle size. The decrease in H_C values with larger V contents (Table 2) suggest that the decrease of magnetic anisotropy is the origin of the observed decrement.

2.2. Cytotoxicity and genotoxicity

The cytotoxic and genotoxic effects of $V_xFe_{3-x}O_4$ MNPs were investigated in the HepG2 cell line (Fig. S7 in Supplementary Material), a common *in vitro* model for toxicological assessments since it expresses the wild-type P53 tumour promotor protein and has retained the activity of several xenobiotic metabolizing enzymes [27,28]. The $V_xFe_{3-x}O_4$ MNPs were tested in the concentration range of 25–100 μm/cm^2, which was selected based on the OECD Study Report and Preliminary Guidance on the Adaptation of the In Vitro micronucleus assay (OECD TG 487) for Testing of Manufactured Nanomaterials from September 2022 [29]. Due to the nature of the suspension of the testes MNPs, which settle on the surface of the cells, the concentrations were calculated per square area

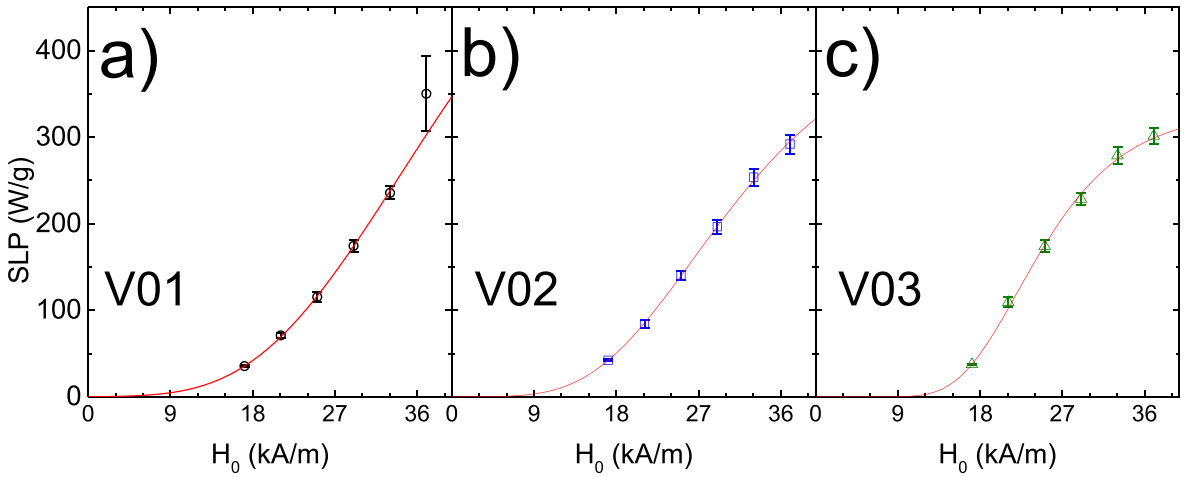

Fig. 7. SLP vs H_0 data at (open symbols) and the fitting curves using Eq. (3) (solid lines) **a)**V01, **b)**V02 and **c)**V03. All data were taken at f = 299.15 kHz.

Table 2
SLP parameters for the low field LRT region $H_0 \lesssim 10\ kA/m$, and the SG model within the complete H_0 range.

Sample	Allometric ($H_0 \lesssim 10\ kA/m$)	Shifted-Gompertz		
	λ	A	k ($\times 10^{-3}$)	HC
V01	2.9 ± 0.1	695 ± 150	5.1 ± 0.6	428 ± 39
V02	2.9 ± 0.1	431 ± 16	7.3 ± 0.2	331 ± 6
V03	2.8 ± 0.1	330 ± 12	12.3 ± 0.7	277 ± 5

rather than per volume. Agglomeration of the nanoparticles was observed in the cell culture medium (Fig. S7), forming large clusters that can potentially affect both internalization mechanisms and the heating efficiency of the MNPs. However, it has been previously reported that this agglomeration of MNPs starts as the particles are in contact with any protein-rich cell culture medium, making this an unavoidable characteristic in most *in vitro* experiments [30]. However, it has also been reported that agglomeration does not impede MNPs internalization in a variety of cell lines, while a proper design of the MNPs to profit from Néel relaxation can preserve their heating efficiency within the intracellular medium [25,31].

The cytotoxicity of the tested $V_xFe_{3-x}O_4$ MNPs was evaluated using the MTT assay. Fig. 8 shows that no significant differences in cell viability occurred after 4h of exposure to the MNPs at any of the tested concentrations (up to 100 μg/cm^2). After 24h of exposure, no significant differences in cell viability were detected for samples V01 and V02 (up to 100 μg/cm^2), while exposure to V03 MNPs significantly reduced the viability of the cells to approximately 64–69 % at all tested concentrations, without any observable dose dependence.

Induction of reactive oxygen species (ROS) following exposure to the tested $V_xFe_{3-x}O_4$ samples was measured using the luminesce ROS-Glo assay, which measures the level of hydrogen peroxide (H_2O_2) within the cells. A statistically significant and dose-dependent increase in ROS formation was observed after exposure to V-01 and V-03 for 4 h (Fig. 9) with V-01 being the most pronounced. Also, the exposure to V-02 resulted in a slight but statistically significant increase in ROS formation at the highest tested concentration (100 μg/cm^2), while a slight decrease in H_2O_2 content was measured at 25 μg/cm^2. These results demonstrated

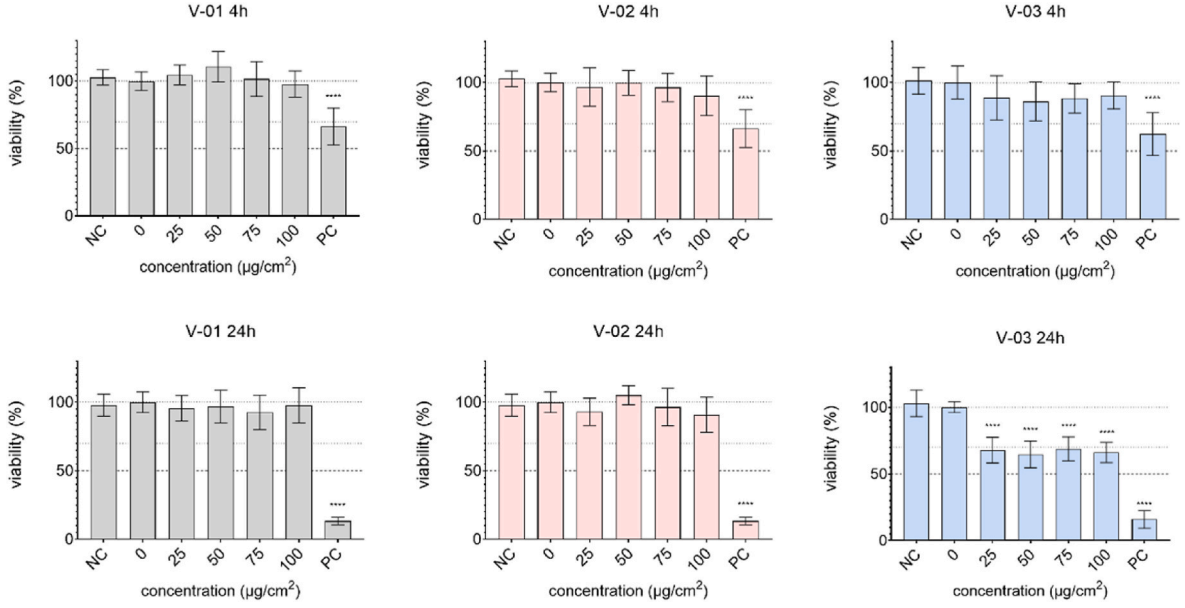

Fig. 8. Cytotoxicity of $V_xFe_{3-x}O_4$ samples for HepG2 cells. Cell viability was determined with the MTT assay after exposure to graded concentrations of the MNPs (V01, V02, and V03) for 4 and 24 h. Data are presented relative to the vehicle control (0; 12% MilliQ water in cell media). NC – cell culture media, PC - 5% DMSO. **** denotes statistically significant difference between the vehicle control and MNPs exposed cells ANOVA; Dunnett's Multiple Comparison test, ****P < 0.0001).

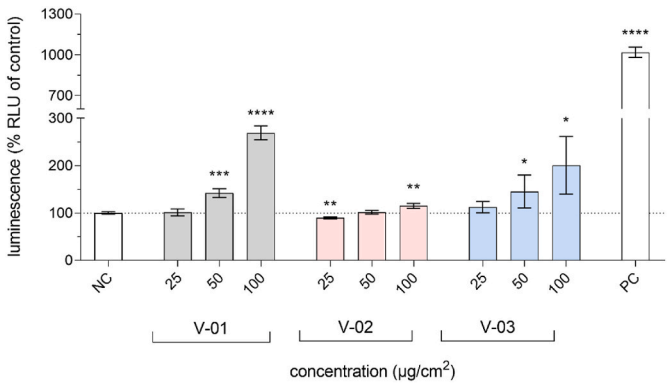

Fig. 9. Reactive oxygen species (ROS) induction by $V_xFe_{3-x}O_4$ samples in HepG2 cells. ROS induction was assessed using the ROS-Glo™ H_2O_2 assay, after the exposure to graded concentrations of the MNPs (V01, V02, and V03) for 4 h and is expressed as the percentage of relative luminescence units (RLU) of the negative control (NC). NC is the negative control (media), and PC is the positive control (0,05 mM TBHP, 20 min). A statistically significant difference (Two-Way ANOVA, and Dunnett's post-test) between MNP-exposed cells and the negative control (cell media) is indicated by *P < 0.05, **P < 0.01, ***P < 0.001 and ****P < 0.0001.

that oxidative stress is one of the possible mechanisms involved in $V_xFe_{3-x}O_4$ nanoparticles activity.

Potential DNA damage induction at the level of the individual cell was investigated using the alkaline comet assay also known as the single cell gel electrophoresis assay (SCGE) [32].

Exposure to the tested MNPs (25–100 µg/cm^2) resulted in a significant dose-dependent increase in DNA damage as detected by the comet assay (Fig. 10). All thee tested MNP samples induced a statistically significant increase in DNA damage to a similar degree already at the lowest concentration tested (25 µg/cm^2), at both exposure times, 4 and 24 h. The comet assay can detect different types of DNA damage, including DNA single-strand (SSBs) and double-strand (DSBs) breaks, alkali-labile sites such as apurinic/apyrimidinic sites, DNA-DNA and DNA-protein cross-links, oxidized and alkylated nucleobases UV-induced cyclobutane pyrimidine dimers and some chemically induced DNA adducts [32–34]. In addition, it can detect transient SSBs, emerging during DNA damage repair [35]. The observed DNA damage could be attributed to the increased levels of ROS, observed after exposure to the MNPs, which could have resulted in oxidative DNA damage and transient lesions due to their elevated repair. Though oxidative stress was confirmed, there might be also other possible mechanisms involved in the observed effects.

Among the different types of DNA damage, DNA DSBs are considered the most deleterious form of DNA damage, as they are inherently more difficult to repair and their induction can potentially promote genomic instability and mutations that can lead to tumorigenesis [35]. The potential influence of the tested MNPs on the genomic instability was evaluated by the Cytokinesis block micronucleus (CBMN) assay, scoring genomic abnormalities specifically in once-divided binucleated (BN) cells including micronuclei (MNi), a biomarker of chromosome breakage (clastogenic effect) and/or whole chromosome loss (aneugenic effect); nuclear buds (NBUDs), a biomarker of elimination of amplified DNA and/or DNA repair complexes; and nucleoplasmic bridges (NPBs), a biomarker of DNA misrepair and/or telomere end-fusions [6]. No significant induction of either form of genomic abnormalities (MNi, NBUDs, or NBPs) was observed after exposure to the tested MNPs (Fig. 11).

To confirm that the tested $V_xFe_{3-x}O_4$ samples do not induce DNA DSBs or have aneugenic activity, the potential induction of DNA DSBs and aneugenic effects were further evaluated by immunofluorescent labelling of the biomarker for DSBs - γH2AX and aneugenicity marker p-H3, and flow-cytometric analysis. When DNA DSBs occur, the event is rapidly followed by phosphorylation of a component of the histone octamer in nucleosomes, histone H2AX. The phosphorylated form γH2AX accumulates at DSBs sites and forms foci that directly correlate with DSBs [36], making γH2AX an important and well established biomarker of DSB induction and clastogenic activity. Histone H3 is phosphorylated during mitosis to allow chromosome condensation and segregation. It is a biomarker of mitotic cells and aneugenic compounds have been shown to induce phosphorylation of histone H3 (p-H3), making p-H3 a strong biomarker for exposure to aneugens [37].

Analysis of the induction of DNA DSBs and p-H3-positive events after exposure to the tested $V_xFe_{3-x}O_4$ MNPs confirmed that none of them, induced the formation of DSBs (Fig. 12a), nor increased the percentage of p-H3 positive events (Fig. 12b), at any of the concentrations tested, which is in line with the results of the CBMN assay, and further confirms that the MNPs did not exhibit clastogenic or aneugenic activity. Therefore, the DNA damage observed with the comet assay was most probably due to the increase in reactive oxygen species generated by the tested MNPs, resulting in oxidative stress and DNA damage. However, the exact causes and mechanisms of action underlying the observed genotoxic effects remain to be determined. Nevertheless, our study confirmed that the tested $V_xFe_{3-x}O_4$ samples did not influence genomic stability or induce genomic abnormalities in HepG2 cells at the test conditions applied, as they did not induce the most deleterious forms of damage at the molecular and genomic level.

3. Conclusions

The findings of this study highlight the promising utility of $V_xFe_{3-x}O_4$ magnetic nanoparticles (MNPs) in the field of biocatalysis, due to their low toxicity and significant heating capabilities, as demonstrated by specific loss power (SLP) values around 400 W/g. A thorough compositional analysis revealed uniform incorporation of vanadium into the crystal lattice, and the presence of multiple vanadium oxidation states suggests that these materials could be versatile in various biocatalytic applications. While our initial data indicate an elevated formation of DNA strand breaks following 4 and 24 h of exposure to $V_xFe_{3-x}O_4$ MNPs, their potential for biomedical applications remains compelling. This assertion is supported by the cytokinesis-block micronucleus (CBMN) assay and flow cytometric analysis of γH2AX and p-H3 markers, which collectively confirm that the tested MNPs did not compromise the genomic stability of HepG2 cells. Specifically, they did not induce major genomic abnormalities such as micronuclei, nuclear buds, or nucleoplasmic bridges (MNIs, NBUDs, and NPBs), nor did they cause DNA double-strand breaks (DSBs) or aneugenic effects—types of damage considered most harmful to cellular genetic material. With proper functionalization and dosage control, the benefits in hyperthermia applications could outweigh the risks, but more in-depth studies are necessary to fully elucidate their safety profile.

4. Methods

4.1. Synthesis of $V_xFe_{3-x}O_4$ nanoparticles

The nanoparticles were synthesized using a method developed by Massart and Cabuil [38], and adapted to form $V_xFe_{3-x}O_4$ nanoparticles. The coprecipitation of VCl_3 and iron (II) ($FeSO_4$) salts was done in the presence of NaOH, and KNO_3 as a mild oxidant, and increasing the amount of Vanadium added to achieve different stoichiometries. First, 135 mL of NaOH buffer (0.8 M) was heated at 95 °C under a N_2 flow in a three-necked quartz flask. In a second step, the precursors $FeSO_4{\cdot}4H2O$ (0.2 M) and VCl_3 (0.1 M) were added to a flask with 15 mL of Milli-Q water. The solution was heated in the quartz flask at 95 °C and kept at that temperature under stirring (200 rpm) for 30 min (Fig. 13). After that time, the particles were washed 2−3 times with deionized water until pH = 6.8−7.2 was reached. Three different samples were synthesized with increasing Vanadium contents at the low-V end of the solid

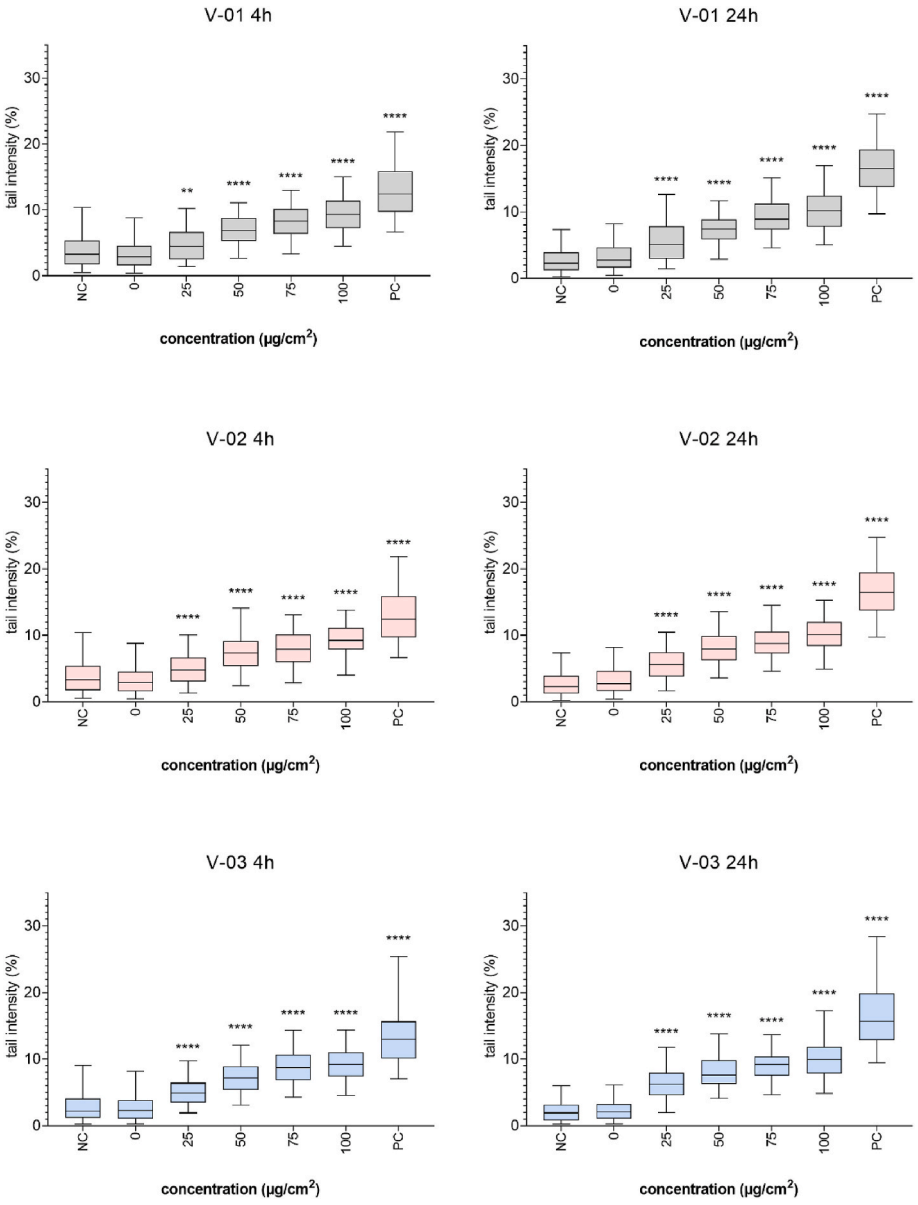

Fig. 10. DNA damage induction by $V_xFe_{3-x}O_4$ samples in HepG2 cells. DNA damage was assessed by the comet assay after the exposure to graded concentrations of the MNPs (V01, V02, and V03) for 4 and 24 h and is expressed as percent of tail DNA. Data are presented as quantile box plots. The edges of the box represent the 25th and 75th percentiles, the median is a solid line through the box, and the error bars represent 95% confidence intervals. PC is the positive control (30 µM BaP). A statistically significant difference (Kruskal-Wallis, and Dunn's post-test) between MNP-exposed cells and the vehicle control (0; 12% MilliQ water in cell media) is indicated by **P < 0.01, and ****P < 0.0001.

solution, with compositions $V_{0.1}Fe_{2.9}O_4$, $V_{0.2}Fe_{2.8}O_4$ and $V_{0.3}Fe_{2.7}O_4$, labelled V01, V02 and V03, respectively (see also Table 1 in Results and Discussion Section).

4.2. Structural and compositional characterization

Structural and phase composition was analysed in powdered samples using a multipurpose diffractometer X-ray diffractometer PANalytical Empyrean®, equipped with PIXcel1D detector in the 10-100° range of 2θ and Cu K_α radiation (λ = 1.5418 Å). Scanning electron microscopy (SEM) images were performed in a SEM-FEG Inspect™ F50 Scanning Electron Microscope using EDS mode and analysed with (INCA Energy® Software, Oxford Instruments®). Observations on dried powder samples covered with a thin layer of carbon (≈20 nm thickness) and energy dispersive X-ray spectroscopy (EDX) analysis (20 kV) was performed to assess the final stoichiometry of the samples.

The MNPs' mass concentration was determined by UV-VIS spectroscopy (Shimadzu® UV Mini 1240) after digestion of the MNPs in acid media, using the absorbance of the iron-thiocyanate complex at λ = 478 nm. The MNPs were dissolved in HCl 6 M and HNO_3 (65%) 1:1 v/v and left for at least 30 min to ensure complete oxidation of Fe to Fe^{3+}. Subsequent addition of potassium thiocyanate (KSCN) 1.5 M results in the formation of the coloured iron-thiocyanate complex. The final MNPs concentration was calculated from EDX using experimental stoichiometry.

X-ray photoelectron spectroscopy (XPS) spectra of the powdered materials were obtained using an AXIS Supra surface analysis instrument (XPS) from Kratos Analytical. Spectra were then fitted and deconvoluted using CasaXPS processing software (Casa Software LTD).

Transmission electron microscopy (TEM) images were taken with a Tecnai T20 (ThermoFisher Scientific) working at 200 kV. Samples were prepared by diluting a suspension of MNPs with Milli Q water or

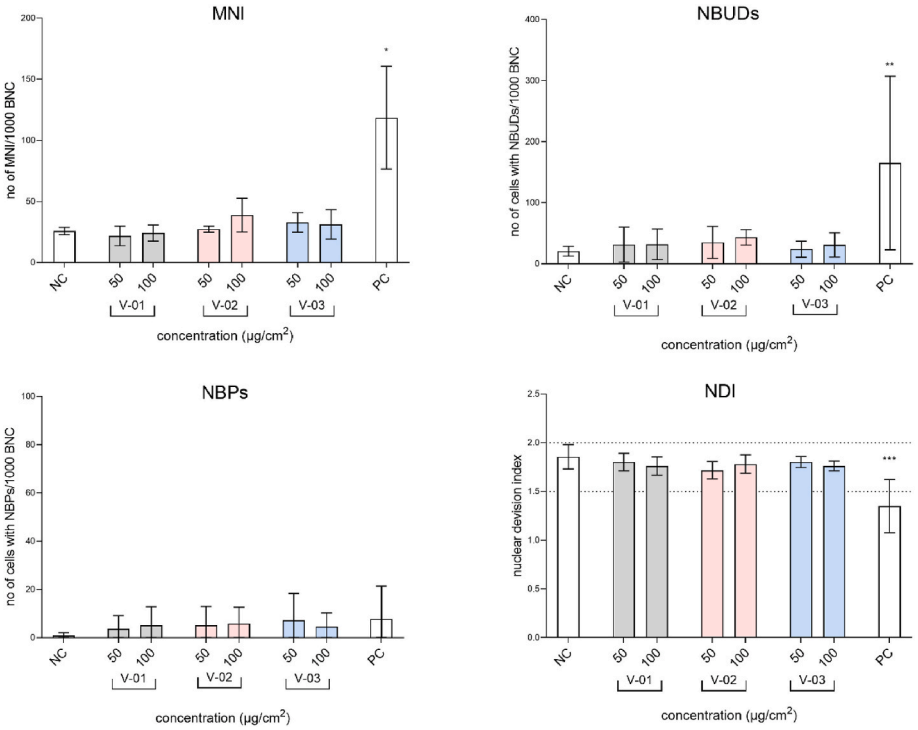

Fig. 11. Influence of MNPs on genomic instability in HepG2 cells. Frequency of MNi, NPBs, and NBUDs in 1000 binucleated cells after 24h of exposure to the tested MNPs. Cells were exposed to graded concentrations of the tested MNPs (V01, V02, and V03) for 24 h. Etoposide (0.5 μM) was used as the positive control (PC), NC is cell culture media. 2000 binucleated cells were counted at each experimental point. A statistically significant difference (ANOVA and Dunnett's post test) between MNP-exposed cells and the NC is indicated by **P < 0.01, and ****P < 0.0001 (ANOVA, and Dunnett's post-test).

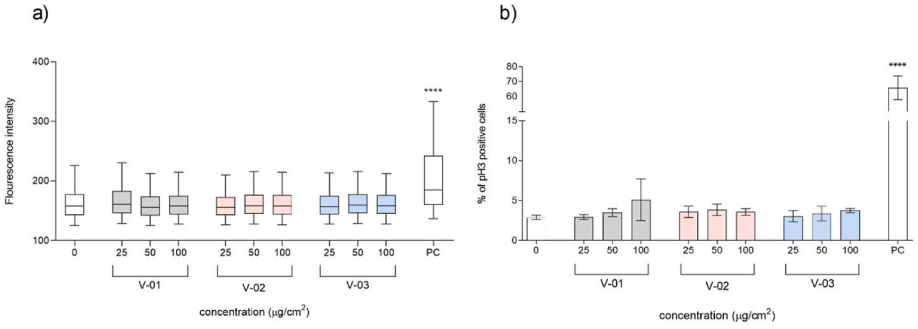

Fig. 12. Potential induction of DNA double-strand breaks (DSBs) and p-H3 positive events by VxFe3-xO4 MNPs in HepG2 cells. a) The fluorescent signal of the APC fluorochrome labelling γH2AX in individual cells, after exposure to graded concentrations (25, 50 and 100 μg/cm^2) of the tested MNPs (V01, V02, and V03) for 24 h, determined by flow cytometry, is shown. Etoposide (0.1 mM) was used as a positive control (PC). Data are presented as quantile box plots. The edges of the box represent the 25th and 75th percentiles, the median is a solid line through the box, and the bars represent 95% confidence intervals. A statistically significant difference (linear mixed-effects model, R program) between MNP-exposed cells and the vehicle control (0; 12% MilliQ water in cell media) is indicated by ****P < 0.0001. b) The average percentage of p-H3-positive events after exposure to graded concentrations (25, 50 and 100 μ g/cm2) of the tested MNPs (V01, V02, and V03) for 24 h, determined by flow cytometry is shown. Colchicine (5 μM) was used as a positive control (PC). A statistically significant difference (ANOVA, and Dunnett's post-test) between MNPs-exposed cells and the vehicle control (0; 12% Milli-Q water in cell media) is indicated by ****P < 0.0001.

ethanol, dropping the suspension onto a carbon-coated copper grid, and left to evaporate at room temperature. The mean size distribution was calculated by measuring the particles from the bright field TEM images with specialized software (Image J). For each sample, N ≈ 300 MNPs were counted, and the number P of bins set for the histogram followed the criterion $P = 1 + ln(N)$. Further analysis at single-particle level was performed by STEM-HAADF images using a Tecnai F30 and Electron energy-loss spectra (EELS) were acquired in a CS-probe-corrected Titan microscope (ThermoFisher® Scientific) at a working voltage of 300 kV using a Tridem® energy filter (Gatan®) spectrometer at an energy dispersion of between 0.1 and 0.5 eV per pixel. Spectrum images were acquired with a 500 ms dwell time and a pixel step size of 0.7 nm. The collection semi angle (b) was 51.3 mrad for a camera length of 10 mm and spectrometer entrance aperture of 1 mm. The convergence semi-angle (a) was 24.8 mrad.

The heating efficiency of the samples was studied by measuring the Specific Loss Power (SLP) of the MNPs. All experiments were performed with MNPs immobilized in gelatin to avoid contributions from Brownian relaxation to the SLP. Measurements were performed in commercial equipment (D5 series, nB nanoscale Biomagnetics, Spain) using a vacuum-insulated sample holder (10^{-6} mbar) within a calorimetric setup. Frequencies within $200 \leq f \leq 800\,kHz$ and fields $10 \leq H_0 \leq 38\,kAm$ were used. From the temperature increase, the SLP was calculated using the relation

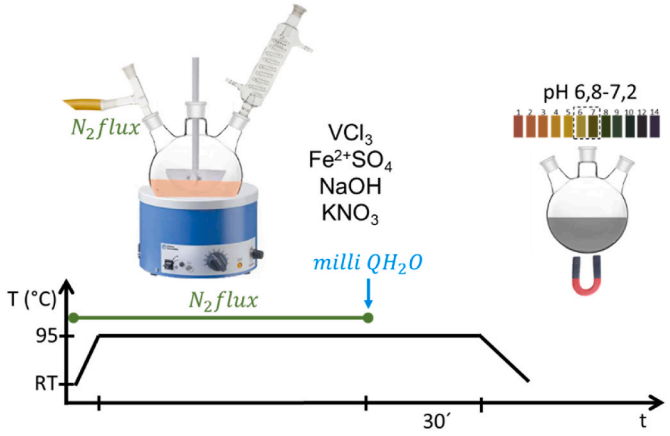

Fig. 13. Schematic presentation of experimental set up and synthesis procedure for $V_xFe_{3-x}O_4$ samples.

$$SLP = \frac{c_l\ \delta_l}{\varphi}\left(\frac{dT}{dt}\right)_{max} \quad \text{Eq. (1)}$$

where c_l and δ_l are the specific heat capacity and the density of the carrier liquid, respectively, and φ the concentration of MNP's in the colloid (in g/L).

The SLP was measured at a fixed alternating magnetic field (AMF) amplitude $H_0 = 37.2\ kA/m$ (468 G) and a frequency $f = 297.70\ kHz$ using the calorimetric method and recording the increase of temperature vs. time for each sample three times (Fig. S1 in the Supplementary Material). The samples were allowed to thermalize at room temperature for ≈10 min until their temperature stabilized, and then the magnetic field was turned on and the resulting temperature variation was recorded. Subsequently, the field dependence of the SLP(H_0) with amplitude H_0 was measured, repeating the T *vs.* time curves multiple times with decreasing field values until there was no noticeable heating in the nanoparticles. The SLP value was calculated for each field using the maximum value of the $\left(\frac{dT}{dt}\right)$ data from the first ≈20 s.

4.3. Toxicological characterization

The *in vitro* cyto- and genotoxicity were assessed (see Fig. 14) in the human hepatocellular carcinoma cell line HepG2 (ATCC-HB-8065™, Manassas, VA, USA). Cells were grown in MEME medium (MEME-10370-047) containing NEAA supplemented with 10% FBS, all from Gibco (Praisley®, Scotland, UK) and 2.2 g/L $NaHCO_3$, 2 mM L-glutamine, 100 IU/mL penicillin/streptomycin and 1 mM sodium pyruvate from Sigma-Aldrich (St. Louis, MO, USA), at 37 °C in a humidified atmosphere with 5% CO_2.

4.4. MTT assay

The cytotoxicity of the of $V_xFe_{3-x}O_4$ samples was evaluated with the MTT (3-(4,5-dimethylthiazol-2-yl)-2,5-diphenyltetrazolium bromide), a colorimetric assay for assessing metabolic activity of cells. Cells were seeded on 96-well plates (Corning Costar Corporation, New York, USA) at a density of 8000 cells/well and allowed to adhere overnight. The

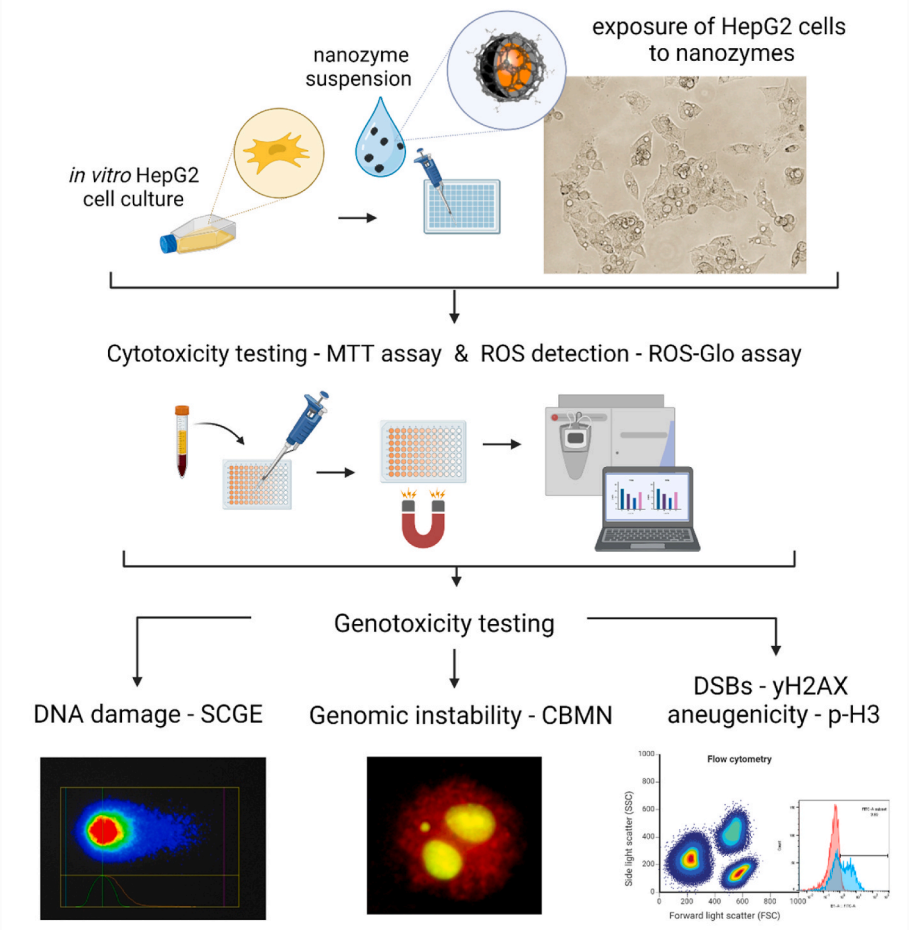

Fig. 14. Illustrative scheme that represents the experimental set up designed for the toxicological characterization of the $V_xFe_{3-x}O_4$ samples.

next day, the cell medium was replaced with a medium containing graded concentrations (0, 25, 50, 75, and 100 μg/cm^2) of the $V_xFe_{3-x}O_4$ samples. DMSO (5%) was used as a positive control. After 4 and 24 h of exposure, MTT (Sigma, St. Louis, USA) was added to each well at a concentration of 0.5 mg/ml, and the reaction mixture was incubated for 3 h. The contents of the wells were then removed, leaving only the cells and the MNPs at the bottom of the wells. DMSO (200 μl, 100%) was added to each well and mixed by pipetting to dissolve the formed formazan crystals. The plate was then placed on a magnetic surface (ferrite Y35 magnets with a holding force of 4.1 kg, Supermagnette. de, Gottmadingen, Germany) and left for 5 min to allow the MNPs to settle and attach to the bottom of the wells. 100 μl of the solution from the top of each well was then carefully transferred to a new plate for spectrophotometric measurement, leaving the MNPs attached to the bottom of the previous plate. Absorbance was measured at 570 and 690 nm (Sinergy MX, BioTek, Winooski, VT, USA). The experiment was performed in five replicates per experimental point and repeated three times independently. A negative control (cell medium), a solvent control (12 % MilliQ water in cell media), and a positive control (5% DMSO) were included in the experiments. Significant differences in cell viability between MNP-exposed cells and the solvent control group were analysed using a One-Way Analysis of Variance (ANOVA) and Dunnett's multiple comparison test in the GraphPad Prism V9 (GraphPad Software, San Diego, CA, USA). Further investigation on the genotoxic activity of $V_xFe_{3-x}O_4$ MNPs was performed through comet assay and cytokinesis block micronucleus (CBMN) assay and by the analysis of γH2AX and H3 positive cells.

4.5. Intracellular ROS detection

The induction of intracellular ROS by $V_xFe_{3-x}O_4$ samples was determined with the ROS-Glo™ H_2O_2 Assay Kit (Promega, Madison, Wisconsin, USA), a homogeneous, rapid, and sensitive luminescent assay that measures the level of hydrogen peroxide (H_2O_2). The assay was performed according to the manufacturer's instructions. Cells were seeded on a 96-well plate (Corning Costar Corporation, New York, USA) at a density of 8000 cells/well and left overnight to attach. The next day, cells were exposed to graded concentrations (25, 50, and 100 μg/cm2) of $V_xFe_{3-x}O_4$ samples together with H_2O_2 Substrate Solution containing H_2O_2 Substrate Dilution Buffer (10 mM) and H_2O_2 Substrate Solution (125 μM). After 4 h of exposure, ROS-Glo™ Detection Solution containing Luciferin Detection Reagent, D-Cysteine, and Signal Enhancer Solution was added to each well, and incubated for 20 min. Within the last 10 min of incubation, the plate was placed on a magnetic surface (ferrite Y35 magnets with a holding force of 4.1 kg, Supermagnette. de, Gottmadingen, Germany) and left for 10 min allowing the MNPs to settle and attach to the bottom of the wells. 100 μl of the solution was then carefully transferred from the top of each well to a new white opaque plate (Thermo Scientific™, Waltham, MA, USA) for luminescence measurement, leaving the MNPs attached to the bottom of the previous plate. Luminescence was measured using a plate-reading luminometer (Synergy HTX, BioTek, Winooski, VT, USA). The experiment was performed in three replicates per experimental point and repeated three times independently. A negative control (cell medium) and a positive control (0,05 mM TBHP, 20 min) were included in the experiments. Significant differences in ROS production between MNP-exposed cells and the negative control group were analysed using Two-Way Analysis of Variance (ANOVA) and Dunnett's multiple comparison test in the GraphPad Prism V9 (GraphPad Software, San Diego, CA, USA).

4.6. Comet assay (SCGE)

DNA damage induction by the $V_xFe_{3-x}O_4$ samples, at the level of the individual cell, was investigated using the alkaline comet assay. Cells were seeded on 12-well plates (Corning, Corning Costar Corporation, NY, USA) at a density of 80 000 cells/well and left to attach overnight. The next day, cell media was replaced with media containing graded concentrations (25, 50, 75 and 100 μg/cm^2) of MNPs. After 4 and 24h of exposure the comet assay was performed as previously described by Møller et al. [32] For the analysis the slides were stained with GelRed nucleic acid stain (Biotium, USA), according to the manufacturer's instructions and scored and analysed under the fluorescent microscope, using the program Comet Assay IV (Instem, Stone, UK). BaP (30 μg/mL) was used as a positive control. Three independent experiments were performed, wherein fifty nuclei were analysed per experimental point. The Kruskal–Wallis nonparametric test and Dunn's multiple comparison test (GraphPad Prism 9) were used to assess statistically significant differences in the percentage of tail DNA between the tested cell populations.

4.7. Cytokinesis block micronucleus (CBMN) assay

The potential influence of the $V_xFe_{3-x}O_4$ samples on genomic instability was evaluated by the Cytokinesis block micronucleus (CBMN) assay. Chromosomal damage events including: micronuclei (MNi), nuclear buds (NBUDs), and nucleoplasmic bridges (NPBs), were scored in once-divided binucleated cells (BNC). Cells were seeded on 12-well plates (Corning Costar Corporation, Corning, NY, USA), with a density of 160.000 cells/well and incubated overnight at 37 °C and 5% CO_2, to attach. They were then exposed to 50 and 100 μg/cm^2 of the tested MNPs, and the CBMN assay was performed after 24h of exposure as previously described by Štraser et al. [39] Etoposide (0.5 μM) was used as a positive control. The Metafer system (Metasystems, Heidelberg, Germany) was used for automatized image acquisition and analysis. The slides were stained with Hoechst 33 342 (Invitrogen, Waltham, MA, USA) for MN, NBUD, and NPB scoring. MNi, NBUDs and NPBs were scored in 2000 BNCs per experimental point. The nuclear division index (NDI) was determined by double staining with Hoechst 33 342 (1:500 in PBS) and acridine orange (20 μg/ml) in 500 cells. Three independent experiments were performed. The Statistically significant differences between MNP-exposed cells and the solvent control group were analysed using ANOVA and Dunnett's multiple comparison test in GraphPad Prism V9.

4.8. Analysis of γH2AX and p-H3 positive cells by flow cytometry

The potential induction of DNA DSBs and p-H3 positive cells, reflecting clastogenic and aneugenic effects, respectively, were evaluated by flow cytometry. Cells were seeded on 6-well plates (Corning Costar Corporation, Corning, NY, USA), at the density of 500.000 cells/plate and left to attach overnight. The next day, the cells were exposed to graded concentrations (25, 50, and 100 μg/cm^2) of MNPs for 24 h and then harvested and fixed in 75% ethanol, as described by Hercog et al. (2019) [40]. Fixed cells were washed with 1x PBS and incubated for 30 min in 1% BSA with 50-fold diluted antibodies against γH2AX pSer139-APC (130-123-256) and pH3-PE (130-105-700) (Miltenyi Biotec, Germany) or REA Control (I)-APC (130-120-709) or REA Control (I)-PE (130-104-613) antibodies (Miltenyi Biotec, Germany) to discriminate unspecific binding of antibodies. Etoposide (0.1 mM) and colchicine (5 μM) were used as positive controls (PC), respectively. Samples were analysed using a flow cytometer - MACSQuant Analyzer 10 with MACSQuantify™ software (Miltenyi Biotech, Germany) and FlowJo V10 software (Becton Dickinson, New Jersey USA). The statistically significant difference in APC fluorescence (γH2AX) between the MNP-exposed and control samples was evaluated in the R program using the linear mixed effects model, while the statistically significant differences in the number of pH3-positive cells between the MNP-exposed and control samples were determined by one-way ANOVA with Dunnett's multiple comparison test, using GraphPad Software V9.

Funding sources

This research was partially funded by Project PDC2021-121 409-I00 (MICRODIAL) MCIN/AEI/10.13039/501100011033 through the European Union "NextGenerationEU"/PRTR", and H2020-MSCA NESTOR project (101007629), the HE CutCancer project (101079113), ARIS P1-0245, ARIS J1-4395 and ARIS MR grant to IR.

CRediT authorship contribution statement

Beatriz Sanz-Sagué: Writing – original draft, Methodology, Investigation, Conceptualization. **Amaia Sáenz- Hernández:** Investigation, Formal analysis, Data curation. **Ana C. Moreno Maldonado:** Supervision, Methodology, Investigation. **Jesús A. Fuentes-García:** Writing – review & editing, Writing – original draft, Software, Formal analysis. **Jorge M. Nuñez:** Software, Methodology, Investigation, Formal analysis. **Bojana Zegura:** Writing – review & editing, Investigation, Funding acquisition, Conceptualization. **Alja Stern:** Writing – review & editing, Supervision, Methodology, Investigation. **Katja Kolosa:** Writing – review & editing, Validation, Methodology. **Iza Rozman:** Writing – review & editing, Methodology, Investigation, Formal analysis, Data curation. **Teobaldo E. Torres:** Writing – review & editing, Investigation, Formal analysis. **Gerardo F. Goya:** Writing – review & editing, Writing – original draft, Supervision, Funding acquisition, Data curation, Conceptualization.

Declaration of competing interest

The authors declare that they do not have any affiliations that would lead to conflicts of interest.

There were no financial or non-financial forms of assistance provided by third parties specifically for the conduct of the research presented in this manuscript.

The authors have had no financial interests or relationships within the past three years that are related to the subject matter of the manuscript, including advisory roles, consulting, equity ownership, or receipt of non-financial support.

None of the co-authors hold any patents or copyrights relevant to the work in this manuscript.

There are no additional activities or relationships that the authors need to disclose, which could be perceived as influencing the research or its interpretation.

Data availability

Data will be made available on request.

Acknowledgments

This research was partially funded by Project PDC2021-121409-I00 (MICRODIAL) MCIN/AEI/10.13039/501100011033 through the European Union "NextGenerationEU"/PRTR", and H2020-MSCA NESTOR project (101007629), the HE CutCancer project (101079113), ARIS P1-0245, ARIS J1-4395 and ARIS MR grant to IR.

Appendix A. Supplementary data

Supplementary data to this article can be found online at https://doi.org/10.1016/j.cbi.2024.110977.

References

[1] L. Néel, Propriétés magnétiques des ferrites; ferrimagnétisme et antiferromagnétisme, in: Annales de physique, 1948.
[2] V. Brabers, Progress in spinel ferrite research, Handb. Magn. Mater. 8 (1995) 189–324.
[3] W. Fontijn, et al., Optical and magneto-optical polar Kerr spectra of Fe 3 O 4 and Mg 2+-or Al 3+-substituted Fe 3 O 4, Phys. Rev. B 56 (9) (1997) 5432.
[4] M.I.A.A. Maksoud, et al., Insights on magnetic spinel ferrites for targeted drug delivery and hyperthermia applications, Nanotechnol. Rev. 11 (1) (2022) 372–413.
[5] M. Amiri, M. Salavati-Niasari, A. Akbari, Magnetic nanocarriers: evolution of spinel ferrites for medical applications, Adv. Colloid Interface Sci. 265 (2019) 29–44.
[6] S. Hussain, et al., Synthesis and characterization of vanadium ferrites, electrochemical sensing of acetaminophen in biological fluids and pharmaceutical samples, Ceram. Int. 49 (5) (2023) 8165–8171.
[7] V.M. Goldschmidt, Die gesetze der krystallochemie, Naturwissenschaften 14 (21) (1926) 477–485.
[8] V.M. Goldschmidt, The principles of distribution of chemical elements in minerals and rocks, in: The Seventh Hugo Müller Lecture, Delivered before the Chemical Society on March 17th, 1937, Journal of the Chemical Society (Resumed), 1937, pp. 655–673.
[9] Y.-L. Chan, S.-Y. Pung, S. Sreekantan, Synthesis of V_2O_5 nanoflakes on PET fiber as visible-light-driven photocatalysts for degradation of RhB dye, Journal of Catalysts 2014 (2014) 370696.
[10] R. André, et al., V2O5 nanowires with an intrinsic peroxidase-like activity, Adv. Funct. Mater. 21 (3) (2011) 501–509.
[11] D.C. Crans, et al., The chemistry and biochemistry of vanadium and the biological activities exerted by vanadium compounds, Chem. Rev. 104 (2) (2004) 849–902.
[12] Y. Shechter, Insulin-mimetic effects of vanadate: possible implications for future treatment of diabetes, Diabetes 39 (1) (1990) 1–5.
[13] K. Werdan, et al., Stimulatory (insulin-mimetic) and inhibitory (ouabain-like) action of vanadate on potassium uptake and cellular sodium and potassium in heart cells in culture, Biochim. Biophys. Acta Biomembr. 687 (1) (1982) 79–93.
[14] S. Kadota, et al., Peroxide (s) of vanadium: a novel and potent insulin-mimetic agent which activates the insulin receptor kinase, Biochem. Biophys. Res. Commun. 147 (1) (1987) 259–266.
[15] S. Tamura, et al., A novel mechanism for the insulin-like effect of vanadate on glycogen synthase in rat adipocytes, J. Biol. Chem. 259 (10) (1984) 6650–6658.
[16] Hussain, S., et al., Synthesis and Characterization of Vanadium Nano-Ferrites and Their Application for Electrochemical Detection of Neurotransmitter Drugs. Synthesis and Characterization of Vanadium Nano-Ferrites and Their Application for Electrochemical Detection of Neurotransmitter Drugs.
[17] W.S. Xi, et al., Cytotoxicity of vanadium oxide nanoparticles and titanium dioxide-coated vanadium oxide nanoparticles to human lung cells, J. Appl. Toxicol. 40 (5) (2020) 567–577.
[18] R. Massart, V. Cabuil, Effect of some parameters on the formation of colloidal magnetite in alkaline-medium - yield and particle-size control, J. Chim. Phys. Phys. Chim. Biol. 84 (7–8) (1987) 967–973.
[19] V. Tsurkan, et al., On the complexity of spinels: magnetic, electronic, and polar ground states, Phys. Rep. 926 (2021) 1–86.
[20] T. Yamashita, P. Hayes, Analysis of XPS spectra of Fe2+ and Fe3+ ions in oxide materials, Appl. Surf. Sci. 254 (8) (2008) 2441–2449.
[21] M.C. Biesinger, et al., Resolving surface chemical states in XPS analysis of first row transition metals, oxides and hydroxides: Cr, Mn, Fe, Co and Ni, Appl. Surf. Sci. 257 (7) (2011) 2717–2730.
[22] E.J. O'Loughlin, M.I. Boyanov, K.M. Kemner, Reduction of vanadium (V) by iron (II)-bearing minerals, Minerals 11 (3) (2021) 316.
[23] M.K. Kuimova, et al., Molecular rotor measures viscosity of live cells via fluorescence lifetime imaging, J. Am. Chem. Soc. 130 (21) (2008) 6672–6673.
[24] D.P. Valdés, et al., Role of anisotropy, frequency, and interactions in magnetic hyperthermia applications: noninteracting nanoparticles and linear chain arrangements, Phys. Rev. Appl. 15 (4) (2021) 044005.
[25] B. Sanz, et al., Low-dimensional assemblies of magnetic MnFe2O4 nanoparticles and direct in vitro measurements of enhanced heating driven by dipolar interactions: implications for magnetic hyperthermia, ACS Appl. Nano Mater. 3 (9) (2020) 8719–8731.
[26] T.E. Torres, et al., The relevance of Brownian relaxation as power absorption mechanism in Magnetic Hyperthermia, Sci. Rep. 9 (1) (2019) 3992.
[27] M. Waldherr, et al., Use of HuH6 and other human-derived hepatoma lines for the detection of genotoxins: a new hope for laboratory animals? Arch. Toxicol. 92 (2018) 921–934.
[28] S. Knasmüller, et al., Use of human-derived liver cell lines for the detection of environmental and dietary genotoxicants; current state of knowledge, Toxicology 198 (1–3) (2004) 315–328.
[29] Development, T.O.f.E.C.a, Study Report and Preliminary Guidance on the Adaptation of the in Vitro Micronucleus Assay (OECD TG 487) for Testing of Manufactured Nanomaterials, 2022. https://www.oecd.org/officialdocuments/publicdisplaydocumentpdf/?cote=env/cbc/mono(2022)15&doclanguage=en.
[30] M.P. Calatayud, et al., The effect of surface charge of functionalized Fe3O4 nanoparticles on protein adsorption and cell uptake, Biomaterials 35 (24) (2014) 6389–6399.
[31] B. Sanz, et al., Magnetic hyperthermia enhances cell toxicity with respect to exogenous heating, Biomaterials 114 (2017) 62–70.
[32] P. Møller, et al., Minimum Information for Reporting on the Comet Assay (MIRCA): recommendations for describing comet assay procedures and results, Nat. Protoc. 15 (12) (2020) 3817–3826.
[33] A. Collins, et al., Measuring DNA modifications with the comet assay: a compendium of protocols, Nat. Protoc. 18 (3) (2023) 929–989.
[34] E. Cordelli, M. Bignami, F. Pacchierotti, Comet assay: a versatile but complex tool in genotoxicity testing, Toxicology Research 10 (1) (2021) 68–78.

[35] A.R. Collins, The comet assay for DNA damage and repair: principles, applications, and limitations, Mol. Biotechnol. 26 (3) (2004) 249–261.
[36] W.M. Bonner, et al., γH2AX and cancer, Nat. Rev. Cancer 8 (12) (2008) 957–967.
[37] C. Prigent, S. Dimitrov, Phosphorylation of serine 10 in histone H3, what for? J. Cell Sci. 116 (18) (2003) 3677–3685.
[38] R. Massart, V. Cabuil, Synthèse en milieu alcalin de magnétite colloïdale: contrôle du rendement et de la taille des particules, Journal de chimie physique 84 (1987) 967–973.
[39] A. Straser, M. Filipic, B. Zegura, Genotoxic effects of the cyanobacterial hepatotoxin cylindrospermopsin in the HepG2 cell line, Arch. Toxicol. 85 (12) (2011) 1617–1626.
[40] K. Hercog, et al., Genotoxic activity of bisphenol A and its analogues bisphenol S, bisphenol F and bisphenol AF and their mixtures in human hepatocellular carcinoma (HepG2) cells, Sci. Total Environ. 687 (2019) 267–276.